

Coordination Regulated Copper Single-Atom Active Sites for Electrochemical Nitrate Reduction to Ammonia

Fan Zhang, Shuo Zhang*, Haoyu Wang, Xingchen Dong, Zunfei Ma, Yuanrong Yang, Tianyu Wang, Liyan Yu, Lifeng Dong*, Lina Sui*

College of Materials Science and Engineering, Qingdao University of Science and Technology, Qingdao 266042, P. R. China.

*Corresponding authors: E-mail: zhangshuo_sd@163.com, donglifeng@qust.edu.cn, lina_sui@qust.edu.cn

1. Experimental details

Synthesis of Cu-NG:

The modified Hummers method was served to obtain GO. Cu-NG was synthesized using a facile two-step method. Briefly, the as-prepared GO powder (100 mg) was dispersed in 68% HNO₃ solution with ultrasonication for 3 h. Then the dispersion was centrifuged and clean with water. The certain concentration of metal salt (CuCl₂) and 100 mg urea were then added into the gained GO suspension (100 mL, 2mg/L) and sonicated for 2 h. The mixed suspension was continuous stirring with 12 h. The obtained suspension was then transferred into Teflon equipped stainless steel autoclave which was hydrothermally treated at 180 °C for 12 h, forming a porous hydrogel. After freeze drying, the resulted production was annealed at 800 °C for 2 h with a heating rate of 10 °C min⁻¹ under Ar (100 sccm) and NH₃ (50 sccm) flowing atmosphere in a quartz tube furnace. Finally, the Cu-NG powder was collected. In addition, we are able to obtain NG catalysts without metal salt.

Characterization:

Morphology observation was conducted within a Zeiss Ultra 55 field emission scanning electron microscope. TEM characterizations were obtained within a FEI Tecnai G2 20 microscope at 200 kV. Atomic-resolution STEM-HAADF images and EELS point spectra were obtained on a double spherical aberration-corrected STEM/TEM FEI Titan G2 60-300 at 300 kV with a field emission gun or on a JEOL Grand ARM with double spherical aberration correctors. XRD data were collected using Rigaku D/MAX 2500 V with Cu K α radiation (1.5418 Å). XPS analysis was performed on an ESCALab MKII spectrometer with Mg K α X-ray as the excitation source. The Raman spectroscopy (Renishaw inVia Raman spectroscope) experiments were performed using a 514 nm laser. N₂ adsorption-desorption isotherms were recorded on an ASAP 2020 accelerated surface area and porosimetry instrument

(Micromeritics), equipped with automated surface area, at 77 K using Barrett–Emmett–Teller calculations for the surface area. XAS spectra at the Cu K-edge were measured at the beamline 1W1B station of the Beijing Synchrotron Radiation Facility (BSRF), China. The Fe and Cu K-edge XANES data were recorded in a fluorescence mode. The concentration of Ion was measured by spectrophotometric analysis (Shimadzu UV-3600 plus).

Differential electrochemical mass spectrometry (DEMS) measurements:

0.1 M KNO₃ with 1 M KOH electrolyte was kept flowing into a specially-made electrochemical cell through a peristaltic pump. Ar was bubbled into the electrolyte constantly before and during the DEMS measurements. A glassy carbon electrode coated with Cu-NG, a Pt wire electrode, and a saturated calomel electrode were used as the working electrode, the counter electrode and the reference electrode, respectively. LSV test was employed from 0.1 to -0.6 V vs RHE at a scan rate of 5 mV s⁻¹ until the baseline kept steady. Then, the corresponding mass signals appeared. After the electrochemical test was over and the mass signal returned to baseline, the next cycle started using the same test conditions to avoid the accidental error during DEMS measurements. The experiment ended after four cycles.

Ion concentration detection methods:

The UV-Vis spectrophotometer was used to detect the ion concentration of pre- and post-test electrolytes after dilution to appropriate concentration to match the range of calibration curves.

Detection of nitrate-N. Firstly, 1.0 mL electrolyte was taken out from the electrolytic cell and diluted to 5 mL to detection range. Then, 0.1 mL 1 M HCl and 0.01 mL 0.8 wt% sulfamic acid solution were added into the aforementioned solution. After 15 minutes, the absorbance was detected by UV-Vis spectrophotometry at a wavelength of 220 nm and 275 nm. The final absorbance of nitrate-N was calculated based on the following equation: $A_{220\text{ nm}} = 2 \times A_{275\text{ nm}}$. The calibration curve can be obtained through different concentrations of KNO₃ solutions and the corresponding absorbance.

Determination of NH₃ using the indophenol blue method. The produced NH₃ was determined by the indophenol blue method. Specifically, the target solution (1 mL) was moved into a clean vessel (5 mL) followed by sequentially adding NaOH solution (1 mL, 1 M) containing salicylic acid (5 wt%) and sodium citrate (5 wt%), NaClO (0.5 mL, 0.05 M), and Na[Fe(NO)(CN)₅] (0.1 mL, 1wt%) aqueous solution. After the incubation for 2 h at room temperature, the mixture was subjected to UV-Vis measurements and resulted in the absorption spectrum (ranged from 500-800 nm). The absorption peak at 655 nm was ascribed to the generated indophenol blue originated from NH₃ in the target solution. To accurately quantify NH₃, concentration-absorbance curves were calibrated using a series of standard

ammonia chloride in KOH solutions (0.1 M). The absorbance of the blank sample without adding the standard NH₃ solution was subtracted from the measured peak absorbance of all tested samples for background correction.

¹⁵N isotope-labelling experiments by ¹H NMR:

¹H NMR spectroscopy (500 MHz) was used to quantify the ¹⁵NH₄⁺/¹⁴NH₄⁺ yield after electrolysis at -0.4 V (vs RHE). The calibration curves with defined ¹⁵NH₄Cl concentrations were constructed as standards. In a typical procedure, 125 µl of the standard solution/electrolytes was first diluted to the detection range and adjust to pH 2.0 by adding 0.1 M HCl. Next, the solution was mixed with 0.1 ml DMSO-*d*6 (hexadeuterodimethyl sulfoxide) (include 0.04 wt% C₄H₄O₄), where DMSO-*d*6 serves as a solvent and C₄H₄O₄ as the internal standard. Finally, the prepared solution was tested by a 500 MHz NMR spectrometer. The NH₃ product peaks area integral ratio to maleic acid were analyzed to confirm the source of NH₃ qualitatively.

Electrochemical in situ FTIR reflection spectroscopy:

Electrochemical in situ FTIR spectroscopy measurements were carried out Nicolet iS20 FTIR spectrometer, equipped with a liquid nitrogen-cooled system. The working electrode, composed of a glassy carbon electrode loaded with catalysts, was vertically pressed onto a CaF₂ window plate to create a thin liquid layer with a thickness of approximately 10 µm. The counter electrode was a platinum foil, and the reference electrode was an Ag/AgCl electrode. The infrared beam was directed nearly perpendicular to the surface of the electrode. The sample spectra were collected within the potential range from 0.1 V to -0.7 V, with steps of 100 mV.

Calculation of the faradaic efficiency and yield rate of NH₃:

The faradaic efficiency (FE) of NH₃ was the percentage of the charge consumed for NH₃ generation in the total charge passed through the electrode according to the equation below:

$$FE(NH_3) = (8 \times F \times C_{NH_3} \times V \times 10^{-16}) / (17 \times Q) \times 100\%$$

The yield rate (YR, mgNH₃ h⁻¹ cm⁻²) of NH₃ can be calculated using the following equation:

$$YR(NH_3) = (C_{NH_3} \times V) / (t \times A) \times 10^{-3}$$

where C_{NH₃} is the measured NH₃ concentration (µg mL⁻¹); V is the volume of the electrolyte; t is the electrolysis time; A is the geometric area of the electrode (1 cm²); F is the faraday constant (96485 C

mol⁻¹); Q (C) is the total charge passed through the electrode; The faradaic efficiency, the yield rate, and corresponding error bars were obtained from three individual samples under the same testing conditions.

2. Electrochemical measurements

Electrocatalytic nitrate reduction:

Electrochemical properties were measured with a VSP Potentiostat (Bio-Logic Corp., France) in an H-type cell with a Nafion membrane (N-117, Dupont) to separate the cathode and anode chambers. In a typical three-electrode system, platinum foil and Hg/HgO (1 M KOH) were used as the reference and counter electrodes, respectively. The working electrode was prepared as follows: 4 mg of catalyst powder, 1 mL DI water and 1 mL ethanol, and 50 μ L Nafion solution (Sigma Aldrich, 5 wt%) were mixed and sonicated for at least 30 min to form a homogeneous ink. Then, a certain volume of uniform catalyst ink was drop-casted onto carbon paper (active area: 1*1 cm⁻²) with a mass loading of 0.24 mg cm⁻² unless specified. Thus, the potentials were converted to the reversible hydrogen electrode (RHE) *via* the following equation: $E_{(RHE)} = E_{(Hg/HgO)} + 0.059 \times pH + 0.098$ V. For electrocatalytic NO₃⁻ reduction, the electrolytes (1 M KOH and 0.1 M KNO₃, unless otherwise specified) were degassed using an ultrapure argon flow to remove O₂ and N₂ and then was evenly distributed to the cathode and anode compartment. The Linear sweep voltammograms (LSV) were performed at a rate of 5 mV s⁻¹. Chronopotentiometry tests were carried out at given potentials to evaluate the faradaic efficiency and yield rate of NH₃. For consecutive recycling test, the Chronopotentiometry tests were performed at -0.4 V vs RHE for a long time with stirring. After electrolysis, the electrolyte was analyzed by UV-Vis spectrophotometry as mentioned below.

Calculation of double-layer capacitance (C_{dl}):

The double-layer capacitance (C_{dl}) was used to determine the ECSA of each electrode according to the reference. To measure the value of C_{dl}, the potential was swept between -0.4 and -0.6V (vs RHE) at varied scan rates. A potential range was selected for the capacitance measurements because no obvious faradaic reactions can be observed in this region. The capacitive currents of $\Delta J_{|J_a-J_c|}@0.15$ V/2 are plotted with respect to the CV scan rates. The data are fitted to a line, whose slope is the C_{dl}. The C_{dl} is proportional to the surface area of electrode.

3. Computational details

The density functional theory (DFT) calculations were performed using the Vienna Ab initio Simulation Package (VASP) code. The exchange-correlation functional in the Perdew-Burke-Ernzerhof (PBE) form within a generalized gradient approximation (GGA) was used. To describe the expansion of the electronic eigenfunctions, the projector-augmented wave (PAW) method was applied with a kinetic energy cutoff of 500 eV. The graphene adopts a 3×3×1 supercell. For structural optimizations, a Γ centered 4×4×1 Monkhorst-Pack k-point sampling was used in the first Brillouin zone, whereas k-point mesh was increased to 8×8×1 for the density of states (DOS) calculations. All atomic positions were fully relaxed until energy and force reached the tolerance of 1×10^{-5} eV and 0.02 eV \AA^{-1} , respectively. The vacuum thickness was set to be 15 \AA to minimize interlayer interactions in this study. The solvation effect was not included since the ignorable energy change was witnessed. Known as a pre- and postprocessing program for the VASP code, VASPKIT was adopted to obtain the DOS diagrams.

The elementary steps of Electrochemical nitrate reduction pathway:

Based on computational hydrogen electrode (CHE) model, The Gibbs free energy (ΔG) calculations of each elementary step can be determined as:

$$\Delta G = \Delta E + \Delta E_{ZPE} - T\Delta S + \Delta U + \Delta pH$$

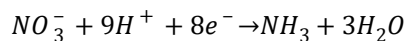
in which ΔE denotes the energy obtained from DFT calculations. ΔZPE and ΔS are the correction of zero-point energy and entropy, respectively. T represents room temperature (298.15 K). The effect of the applied electrode potential and pH are contained by the correction of ΔU and ΔpH , respectively.

To avoid calculating the energy of charged NO_3^- directly, gaseous HNO_3 is chosen as a reference instead. The adsorption energy of NO_3^- ($\Delta G^*_{\text{NO}_3}$) is described as

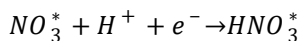
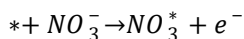
$$\Delta G^*_{\text{NO}_3} = G^*_{\text{NO}_3} - G^* - G_{\text{HNO}_3(\text{g})} + 1/2G_{\text{H}_2(\text{g})} + G_{\text{correct}}$$

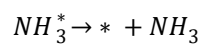
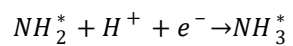
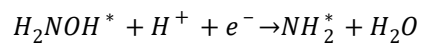
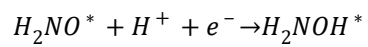
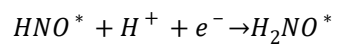
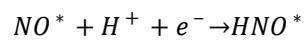
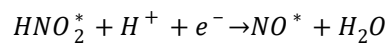
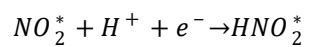
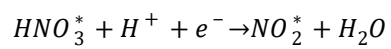
where $G^*_{\text{NO}_3}$, G^* , $G_{\text{HNO}_3(\text{g})}$, and $G_{\text{H}_2(\text{g})}$ are the Gibbs free energy of NO_3 adsorbed on substrate, HNO_3 , and H_2 molecules in the gas phase, respectively. $\Delta G_{\text{correct}}$ denotes the correction of adsorption energy and is set to 0.392 eV.

Electrochemical reduction of nitrate results in the formation of NH_3 with nine protons and eight electrons transferred. The whole reaction can be summarized as:



the elementary steps of reduction pathway on catalyst were simulated according to the following reactions:





where * represents the adsorption site.

Figures

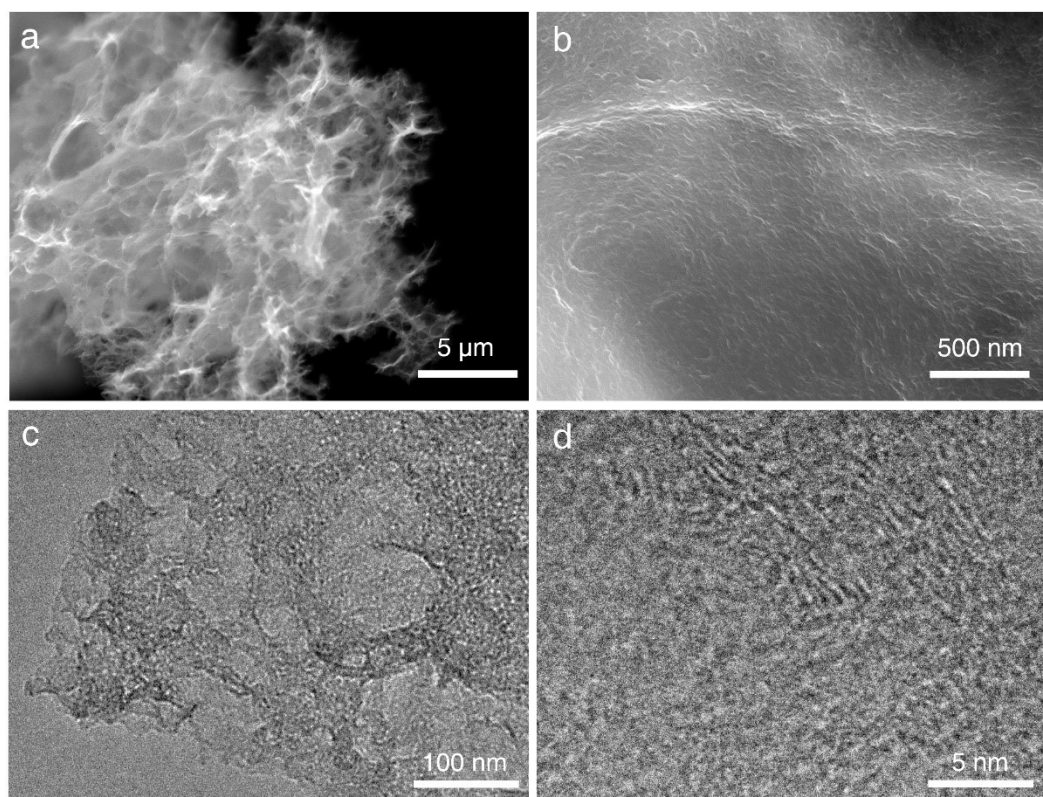


Fig. S1. (a, b) SEM and (c, d) TEM images of NG. The rGO layer presents a broad and flat surface, while NG develops a porous structure. During the hydrothermal and annealing processes, the introduction of a Cu precursor facilitates the loading of Cu single atoms onto the nitrogen edges within the micropores.

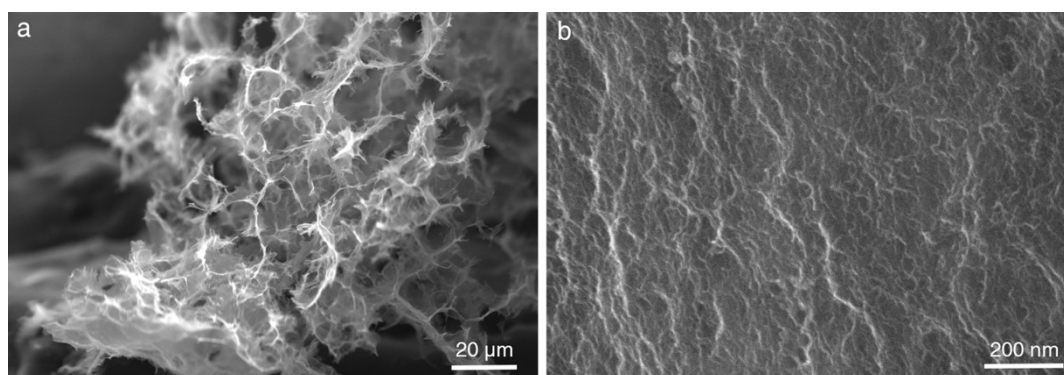


Fig. S2. SEM images of Cu-NG, indicating Cu-NG has an interconnected vesicle-like structure.

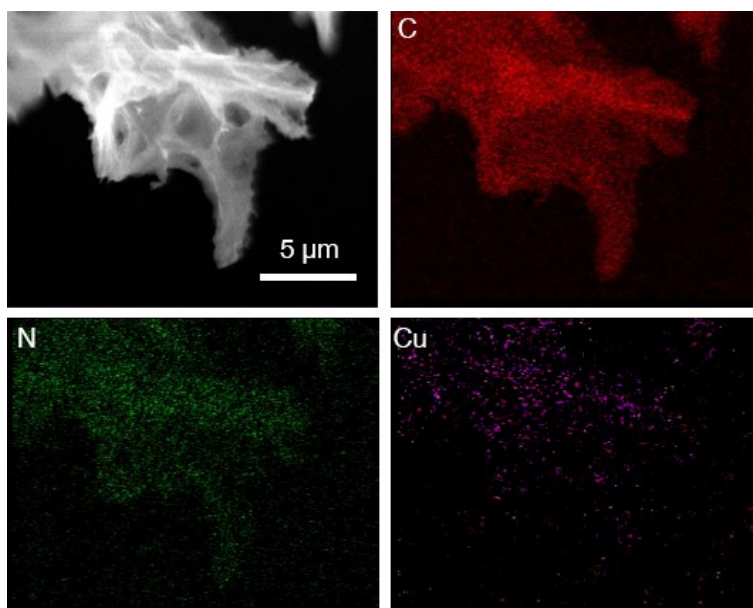


Fig. S3. EDS mapping images of Cu-NG, indicating the existence of Cu, N, and C elements throughout the graphene layer.

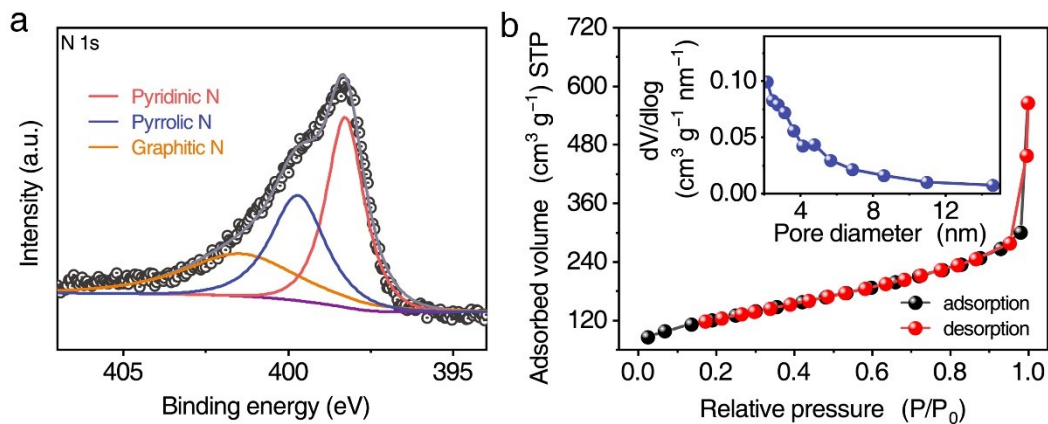


Fig. S4. (a) High-resolution N 1s XPS spectrum of NG. The broad peak of N 1s signal could be deconvoluted to pyridinic N at ~ 398.3 eV (40.6% of N species), pyrrolic N at ~ 400.2 eV (32.3% of N species), and graphitic N at ~ 401.4 eV (27.1% of N species). (b) N₂ adsorption–desorption isotherms of NG (inset: corresponding pore-size distribution). The N₂ adsorption-desorption isotherms of NG reveal the existence of a predominantly mesoporous structure. The pore size distribution exhibits a prominent peak in the range of 2-4 nm. Using the Brunauer–Emmett–Teller (BET) method, the surface area is calculated to be 876 m² g⁻¹, which is similar with Cu-NG.

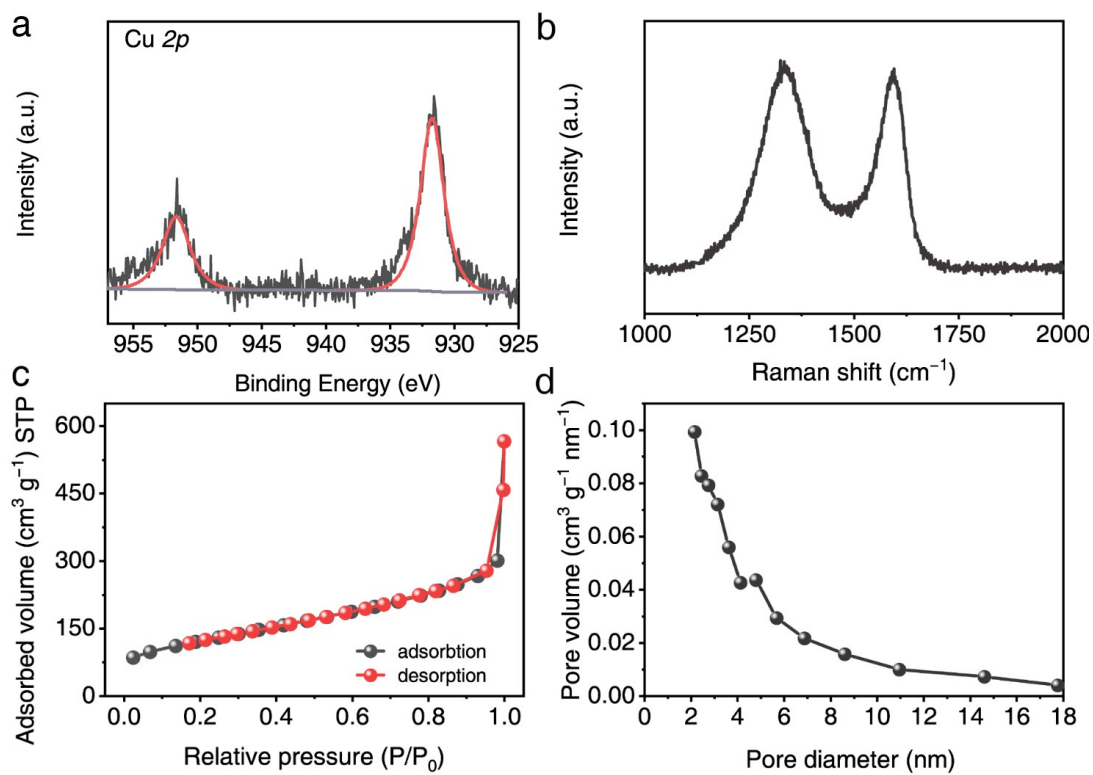


Fig. S5. (a) High resolution XPS of Cu 2p spectra in Cu-NG, (b) Raman spectra of Cu-NG, the I_D/I_G is 1.01, (c) N_2 adsorption-desorption isotherms and (d) The pore-size distribution curve of Cu-NG.

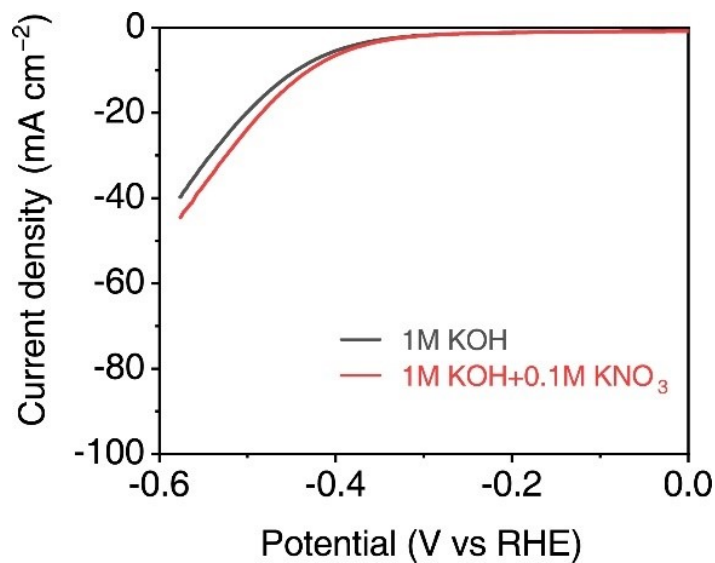


Fig. S6. LSV curves of NG in the electrolyte of 1 M KOH and 0.1 M KNO₃.

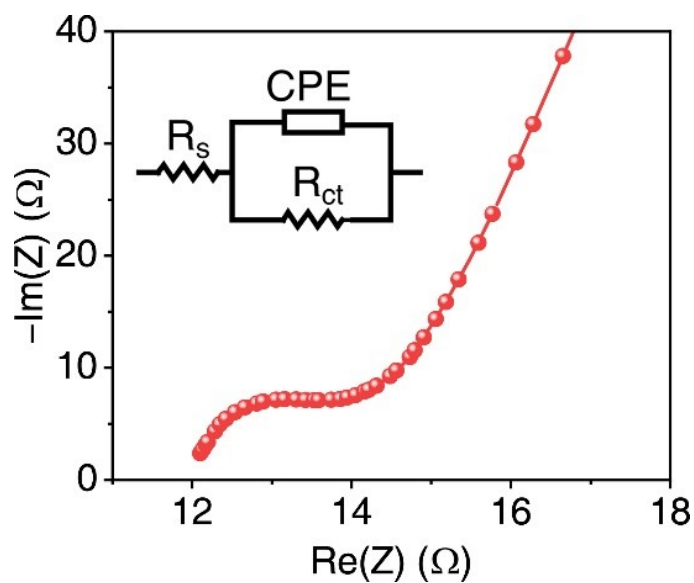


Fig. S7. Nyquist plot of Cu-NG electrodes. The EIS spectra were fitted using Randles equivalent circuit model (illustrated in the inset), yielding the charge transfer resistance (R_{ct}) of 2.38Ω for the Cu-NG.

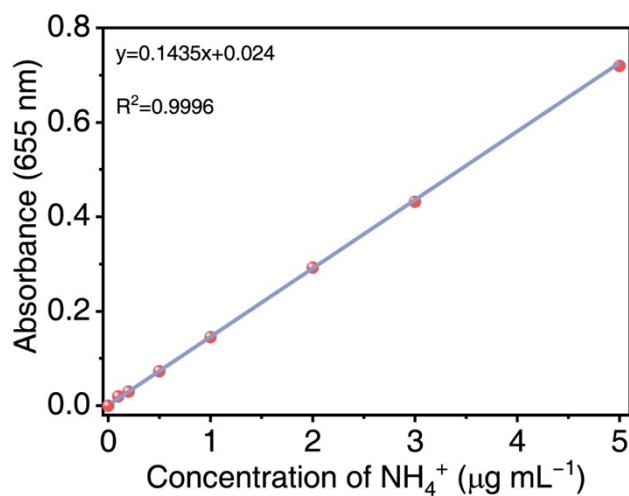


Fig. S8. Calibration curve of NH_4^+ for different concentrations using ammonium chloride solutions of known concentration as standards.

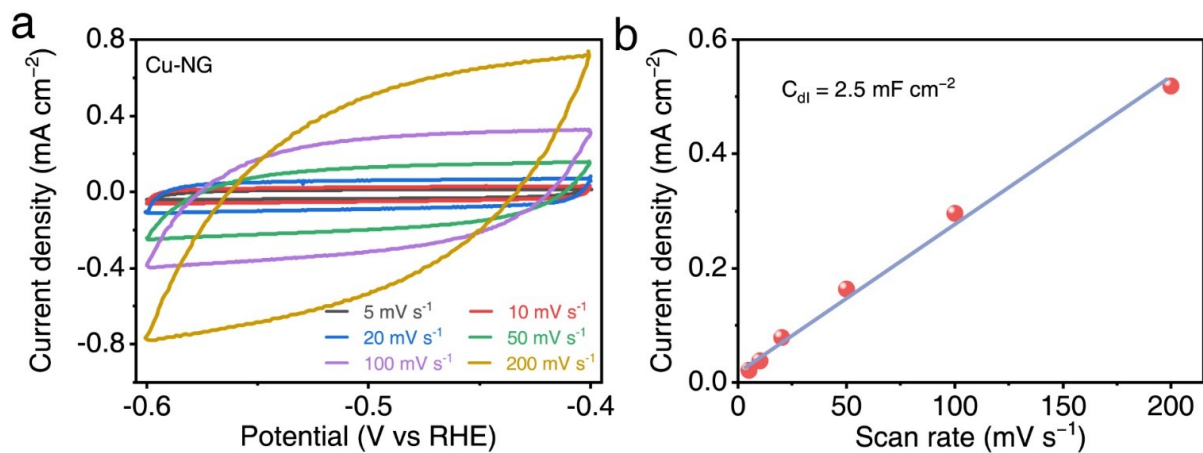


Fig. S9. Cyclic voltammograms for (a) Cu-NG catalysts at different scan rates from 5 to 200 mV s⁻¹, respectively. The C_{dl} plots for extraction electrochemical surface area (ECSA) of (b) Cu-NG.

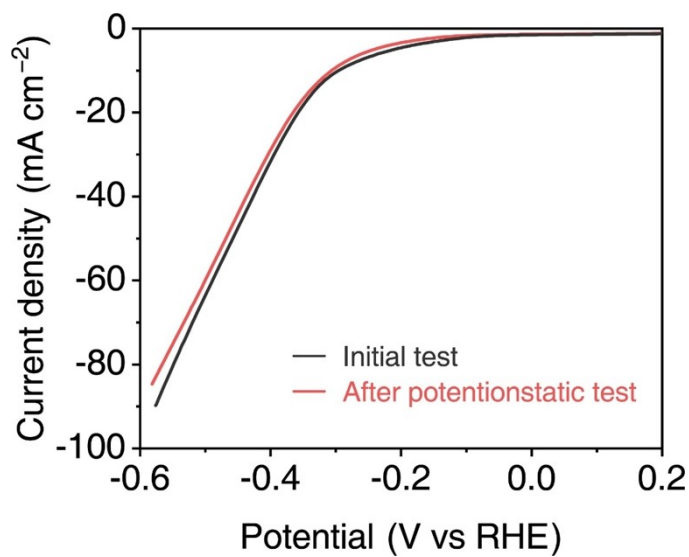


Fig. S10. LSV curves of the initial and after 24 h test of Cu-NG.

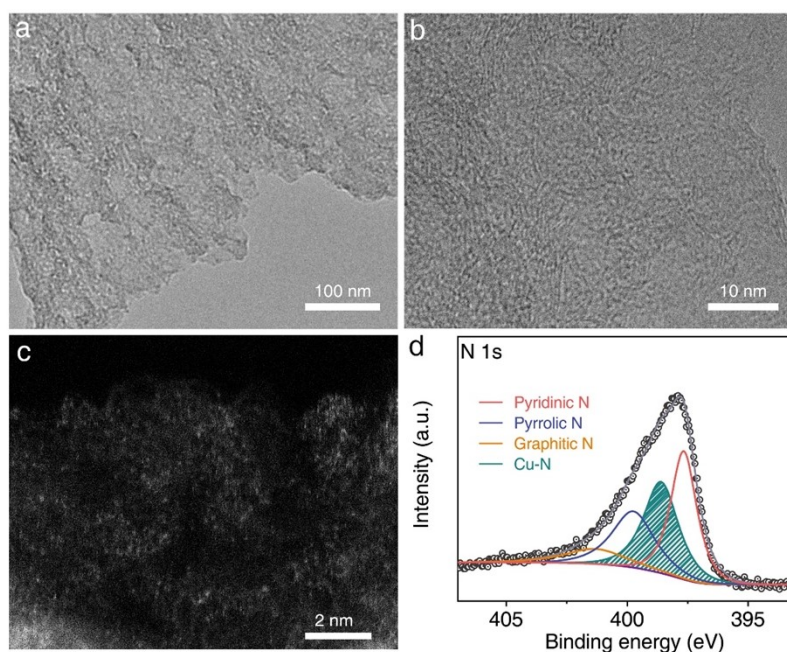


Fig. S11. (a) TEM, (b) HRTEM, (c) HAADF-STEM images and (d) High-resolution N 1 s XPS spectrum of Cu-NG after 24 h test.

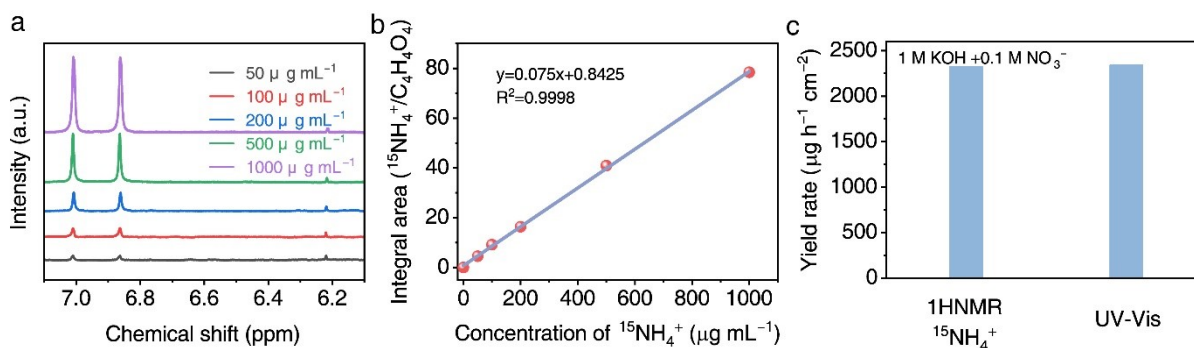


Fig. S12. (a) ^1H NMR spectra of $^{15}\text{NH}_4^+$ ions at different concentrations. $\text{C}_4\text{H}_4\text{O}_4$ with a constant concentration was used as an external standard (with the proton signal at $\delta = 6.25$ ppm). (b) Calibration curve for $^{15}\text{NH}_4^+$ detection using ^1H NMR. (c) Comparison of the ammonia yield rate over Cu-NG quantified by the ^1H NMR and UV-vis spectra.

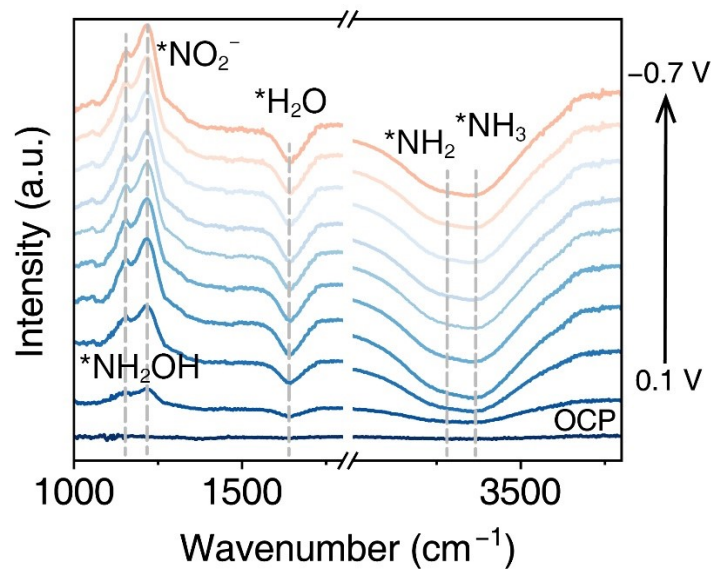


Fig. S13. In situ FTIR of Cu-NG from 0.1 to -0.7 V vs. RHE. Dotted lines represent the peak position.

Tables

Table S1. EXAFS structure parameters from the Cu-NG.

K-edge	Shell	N	$r/\text{\AA}$	$\sigma^2/10^{-3}\text{\AA}^2$	R
Cu	Cu-N	2.03	1.50 ± 0.021	6.41 ± 0.35	0.03

N : coordination number;

r : bond length;

σ^2 : Debye-Waller factor (disorder);

R : R-factor.

Table S2. Reported catalysts for the nitrate reduction to ammonia.

Materials	Maximum FE to NH ₃	Corresponding potential to NH ₃	Maximum NH ₃ yield rate	Electrolyte conditions	Ref
Cu-NG	91%	-0.4 V vs RHE	3600 $\mu\text{g h}^{-1} \text{cm}^{-2}$ -0.5 V vs RHE	0.10 M KNO ₃ , 1.0 M KOH, pH=14	This work
In ₁ Cu	95.1%	-0.6 V vs RHE	11050 $\mu\text{g h}^{-1} \text{cm}^{-2}$ -0.7 V vs RHE	0.5 M Na ₂ SO ₄ , 0.1 M NaNO ₂ , PH=7	1
Cu-N ₁ O ₂ SACs	96.5%	-0.6 V vs RHE	4600 $\mu\text{g h}^{-1} \text{cm}^{-2}$ -1.0 V vs RHE	0.01 M KNO ₃ , 0.1 M KOH, pH=13	2
Cu/Cu ₂ O/HT C-350	89.5%	-0.95 V vs RHE	1581 $\mu\text{g h}^{-1} \text{mg}_{\text{cat}}^{-1}$ -0.95 V vs RHE	0.5M Na ₂ SO ₄ , 200 ppm NaNO ₃ , pH=7	3
Cu/Cu ₂ O	91.1%	-0.6 V vs RHE	6500 $\mu\text{g h}^{-1} \text{cm}^{-2}$ -0.8 V vs RHE	0.5 M PBS, 100 mg L ⁻¹ NO ₃ ⁻ N, pH=7	4
Co-Cu SCC	91.2%	-0.3 V vs RHE	185300 $\mu\text{g h}^{-1} \text{g}_{\text{cat}}^{-1}$ -0.5 V vs RHE	0.10 M KNO ₃ , 0.10 M KOH, pH=13	5
Cu-N ₄ B ₂	98.2%	-0.6 V vs RHE	7480 $\mu\text{g h}^{-1} \text{cm}^{-2}$ -0.7 V vs RHE	0.10 M KNO ₃ , 1.0 M KOH, pH=14	6

Cu/Cu ₂ O/Pi NWs	96.6%	-0.5 V vs RHE	8190 $\mu\text{g h}^{-1}\text{cm}^{-2}$ -0.5 V vs RHE	0.10 M KNO ₃ , 1.0 M KOH, pH=14	7
Cu/Cu ₂ O/Cu O	90.52%	-0.23 V vs RHE	2040 $\mu\text{g h}^{-1}\text{cm}^{-2}$ -0.23 V vs RHE	500 ppm KNO ₃ , 1.0 M KOH, pH=14	8
CuIr	93.0%	-0.22 V vs RHE	10251 $\mu\text{g h}^{-1}\text{cm}^{-2}$ -0.27 V vs RHE	0.10 M KNO ₃ , 1.0 M KOH, pH=14	9
VO _{2-x} /CuF	77.9%	-1.3 V vs RHE	3116 $\mu\text{g h}^{-1}\text{cm}^{-2}$ -1.3 V vs RHE	1.5 mmol KNO ₃ 0.1 M K ₂ SO ₄ pH=7	10
Cu NNs-B	98.1%	-0.6 V vs RHE	306 $\mu\text{g h}^{-1}\text{cm}^{-2}$ -0.6 V vs RHE	0.5 M Na ₂ SO ₄ , 100 mg L ⁻¹ NO ₃ ⁻ N, pH=7	11
RuSA@Cu ₂₊₁ O	98.02%	-0.4 V vs RHE	1377 $\mu\text{g h}^{-1}\text{cm}^{-2}$ -0.4 V vs RHE	0.10 M KNO ₃ , 0.10 M KOH, pH=13	12
7Cu3FeOx/A C	76%	-0.8 V vs RHE	4800 $\mu\text{g h}^{-1}\text{mg}_{\text{cat}}^{-1}$ -1.1 V vs RHE	0.5 mol/L Na ₂ SO ₄ , 16 mmol/L KNO ₃ , PH=7	13
Fe- CuO@Co ₃ O ₄ / CC	84.4%	-1.2 V vs RHE	8005 $\mu\text{g h}^{-1}\text{g}^{-1}$ -1.2 V vs RHE	0.1 M Na ₂ SO ₄ , 0.01 M NaNO ₃ , PH=7	14
Ni ₂ P@Cu ₃ P	96.97%	-0.49 V vs RHE	4732.8 $\mu\text{g h}^{-1}\text{cm}^{-2}$ -0.49 V vs RHE	0.5 M K ₂ SO ₄ , 200 ppm KNO ₃ , PH=7	15
Cu ₃ P@Co(O H) ₂ /CF	86.7 %	-0.17 V vs RHE	3400 $\mu\text{g h}^{-1}\text{cm}^{-2}$ -0.37 V vs RHE	0.01 M KNO ₃ , 1.0 M KOH, PH=14	16
ED- 30PANI@B- Cu	96.1%	-0.89 V vs RHE	5100 $\mu\text{g h}^{-1}\text{cm}^{-2}$ -0.89 V vs RHE	0.5 M K ₂ SO ₄ , 200 ppm KNO ₃ , PH=7	17

Cu _x O/Ti ₃ C ₂ T _x	48%	-0.7 V vs RHE	44000 μg h ⁻¹ mg _{cat} ⁻¹ -0.8 V vs RHE	0.1 M K ₂ SO ₄ , 0.5 M KNO ₃ , PH=7	18
Cu@CuTCN Q	96.4%	-0.6 V vs RHE	3995 μg h ⁻¹ cm ⁻² -0.9 V vs RHE	0.1 M KNO ₃ , 0.1 M KOH, PH=13	19
Cu ₃ N/GDY	98.1%	-0.9 V vs RHE	35280 μg h ⁻¹ mg _{cat} ⁻¹ -0.9 V vs RHE	0.1 M KNO ₃ , 1.0 M KOH, PH=14	20

References

1. F. Wang, S. Shang, Z. Sun, X. Yang, and K. Chu, *Chemical Engineering Journal*, 2024, **489**, 151410.
2. Z. Gu, Y. Zhang, Y. Fu, D. Hu, F. Peng, Y. Tang, and H. Yang, *Angewandte Chemie*, 2024, **136**, 202409125.
3. A. Ma, X. Wu, X. Li, Y.D. Susanti, D. Liu, H. Li, A.T. Kuvarega, B.B. Mamba, and J. Gui, *Applied Surface Science*, 2024, **653**, 159397.
4. Y. Li, L. Fang, and Y. Bai, *Energies*, 2024, **17**, 4467.
5. J. Suh, H. Choi, Y. Kong, and J. Oh, *Advanced Science*, 2024, **11**, 2407250.
6. T. Huang, T. Liang, J. You, Q. Huo, S. Qi, J. Zhao, N. Meng, J. Liao, C. Shang, and H. Yang, *Energy & Environmental Science*, 2024, **17**, 8360-7.
7. W. Luo, Z. Guo, L. Ye, S. Wu, Y. Jiang, P. Xu, H. Wang, J. Qian, X. Zhou, and H. Tang, *Small*, 2024, 2311336.
8. N. Dong, J. Wu, D. Wu, G. Jiang, J. Shi, and S. Chang, *ACS Applied Nano Materials*, 2024, **7**, 9269-77.
9. X. Guo, J. Yu, S. Ren, R.-T. Gao, L. Wu, and L. Wang, *ACS nano*, 2024, **18**, 24252-61.
10. S. Mahmood, A. Bilal, M. Ammar, S. Khan, N. Afshan, O. Alduhaish, N. Hassan, G.A. Ashraf, A. Bahadur, and K.L. Fow, *Journal of Power Sources*, 2024, **608**, 234644.
11. Q. Wu, X. Fan, K. Liu, X. Quan, and Y. Liu, *Applied Catalysis B: Environment and Energy*, 2025, **361**, 124597.
12. Y. Lin, Y. Wang, Y. Xu, H. Liu, X. Liu, L. Shan, C. Wu, L. Yang, and L. Song, *Advanced Functional Materials*, 2024, 2417486.
13. Y. Xie, X. Cheng, W. Yang, C. Yan, and S. Wu, *Journal of Electroanalytical Chemistry*, 2024, **972**, 118633.

14. B. Zhang, J. Zhao, H. Qiu, M. Chen, X. Ren, H. Wang, and Q. Wei, *ChemPhysChem*, 2024, **25**, 202400738.
15. S. Lv, F. Gou, H. Wang, Y. Jiang, W. Shen, R. He, and M. Li, *Applied Surface Science*, 2024, **648**, 159082.
16. J. Yue, S. Liping, W. Yuechen, H. Lihua, and Z. Hui, *International Journal of Hydrogen Energy*, 2024, **71**, 820-30.
17. Y. Li, Y. Pu, Z. Yan, Y. He, R. Deng, H. Li, T. Duan, and Y. Zhang, *Journal of Environmental Chemical Engineering*, 2024, **12**, 112627.
18. S. Ingavale, P. Marbaniang, M. Palabathuni, and N. Mishra, *Nanoscale Advances*, 2024, **6**, 481-8.
19. N. Zhou, J. Wang, N. Zhang, Z. Wang, H. Wang, G. Huang, D. Bao, H. Zhong, and X. Zhang, *Chinese Journal of Catalysis*, 2023, **50**, 324-33.
20. Z. Zhang, X. Feng, Z. Zhang, L. Chen, W. Liu, L. Tong, X. Gao, and J. Zhang, *Journal of the American Chemical Society*, 2024, **146**, 14898-14904.